Contents lists available at ScienceDirect

Applied Catalysis B: Environmental

Synergetic activation of peroxymonosulfate by Co_3O_4 modified g-C_3N_4 for enhanced degradation of diclofenac sodium under visible light irradiation

Huixin Shao [a,b], Xu Zhao [a,b,*], Yanbin Wang [a], Ran Mao [a], Yan Wang [a], Meng Qiao [a], Shen Zhao [a], Yongfa Zhu [c]

[a] Key Laboratory of Drinking Water Science and Technology, Research Center for Eco-Environmental Sciences, Chinese Academy of Sciences, Beijing 100085, PR China
[b] University of Chinese Academy of Sciences, Beijing 100049, PR China
[c] Department of Chemistry, Beijing Key Laboratory for Analytical Methods and Instrumentation, Tsinghua University, Beijing, 100084, PR China

ARTICLE INFO

ABSTRACT

Co_3O_4 nanoparticles modified g-C_3N_4 composites (Co_3O_4-g-C_3N_4) were prepared and used as a visible light responsive photocatalyst for the removal of diclofenac sodium (DCF). The Co_3O_4-g-C_3N_4 with 0.20% Co_3O_4 loading exhibited the highest photocatalytic activity towards DCF degradation among the various Co_3O_4 loading. In the presence of peroxymonosulfate (PMS), the removal efficiency of DCF with an initial concentration of 10 mg/L was greatly increased from 20% to 100% within 30 min and the first order-kinetic constant was increased from 0.00469 to 0.08403 min^{-1}. Influencing factors including DCF concentrations, PMS concentrations, and initial pH values were investigated in details. Low pH value was favorable to DCF degradation. Reactive oxygen species generated in the photocatalytic process were identified by radical quenching tests and electron spin response. It was proposed that both sulfate and hydroxyl radicals contributed to the degradation of DCF. PMS could be activated by photogenerated electrons from the Co_3O_4-g-C_3N_4 hybrids under visible light, as well as the Co_3O_4 itself to generate sulfate radicals jointly. Hydroxyl radicals were generated from the reaction between sulfate radicals and H_2O/OH$^-$. As a result, DCF was efficiently degraded.

© 2017 Published by Elsevier B.V.

1. Introduction

Recently, sulfate radicals-based advanced oxidation processes (AOPs) have attracted more and more attention. In this process, activation of persulfate ($S_2O_8^{2-}$, PS) or peroxymonosulfate ions (HSO$_5^-$, PMS) can generate sulfate radicals (SO$_4^{•-}$, E^0(SO$_4^{•-}$/SO$_4^{2-}$) = 2.5–3.1 V$_{NHE}$); Its redox potential is even higher than hydroxyl radicals (•OH, E^0(•OH/H$_2$O) = 1.8–2.7 V$_{NHE}$) [1–3]. Most of the organic pollutants can be efficiently degraded. It is recognized that PMS and PS can be activated by transition metal ions [1], heat, and UV [3] to generate SO$_4^{•-}$. Generally, UV and thermal activation processes need an additional energy [4]. The transition metal ions such as Co(II) and Cu(II) ions can efficiently activate PMS into SO$_4^{•-}$. However, in this process, the metal ions should be carefully removed.

Recently, the heterogeneous activation of PMS has been largely investigated [5,6]. Transitional metal oxides, such as Co$_3$O$_4$, Mn$_2$O$_3$ and Mn$_3$O$_4$, possess the catalytic activity for the activation of PMS due to their redox cycle (e.g. Mn^{2+}/Mn^{3+}, Mn^{3+}/Mn^{4+} and Co^{2+}/Co^{3+}). For example, α-Mn$_2$O$_3$ was used as heterogeneous catalyst to activate PMS [7]. Differently, Co$_3$O$_4$, with band gap energy of 2.1 eV, can activate PMS by chemical redox as well as photocatalysis process. However, cobalt ions are easily released from Co$_3$O$_4$ and photocatalysis activation process is limited by the separation efficiency of photogenerated charges [8]. Therefore, to improve its catalytic activity and stability, Co$_3$O$_4$ was loaded onto various supports such as graphene, TiO$_2$, SiO$_2$, zeolite, Bi$_2$O$_3$, coal fly ashes and mesoporous g-C$_3$N$_4$ [9–11]. Titanate supported cobalt catalysts can activate PMS by photogenerated electrons to generate SO$_4^{•-}$ and the removal efficiency of phenol is greatly enhanced compared to the simple photocatalysis [12].

Graphitic carbon nitride (g-C$_3$N$_4$) has two-dimensional planes of tri-s-triazine and π-conjugated phase between the layers, and has exhibited photocatalytic, electrocatalytic, and heterogeneous catalytic activities [13]. Most of the studies focused on water

splitting and hydrogen production under visible light irradiation [13–15]. Application of g-C_3N_4 for organic contaminants degradation was also reported [16,17]. Generally, its photocatalytic activities toward contaminants degradation are desired to be increased due to its weak oxidation ability. The semiconductor coupling can enhance the photocatalytic activity of g-C_3N_4 by accelerating the separation of photogenerated charges [15]. Moreover, it was also reported that g-C_3N_4 could activate PMS by the photogenerated electrons under visible light to produce $SO_4^{\bullet-}$ and 100% AO7 could be removed within 30 min [18].

The composites of Co_3O_4-g-C_3N_4 have been studied. The catalytic ability of Co_3O_4 for CO oxidation was enhanced by mesoporous g-C_3N_4 due to improved surface areas, increased Co^{3+} and lattice oxygen contents of Co_3O_4. However, the photocatalysis of composites was not involved [11]. It was reported that photogenerated charges, $^\bullet O_2^-$ and $^\bullet OH$ are the main active species in photocatalysis process [19–21]. For example, Co_3O_4-g-C_3N_4 hybrids exhibited higher photocatalytic properties due to the $^\bullet O_2^-$ and photogenerated holes. However, it was still required 3 h to achieve 100% removal of methyl orange [22]. The photocatalysis process could be enhanced with the addition of PMS [8,12,18]. To the best of our knowledge, no work has been performed on the Co_3O_4-g-C_3N_4 hybrids for the heterogeneous activation of PMS. Herein, the prepared Co_3O_4-g-C_3N_4 composites were used to activate PMS under visible light irradiation for the removal of DCF. In comparison with individual Co_3O_4 or g-C_3N_4, a synergetic degradation of DCF was observed. PMS could be activated by photogenerated electrons from the Co_3O_4-g-C_3N_4 hybrids under visible light irradiation. Co_3O_4 not only accelerated the separation of photogenerated charges of Co_3O_4-g-C_3N_4 composites but also activated the PMS by itself. These combined processes were responsible for the efficient degradation of DCF.

2. Experimental section

2.1. Materials

All chemicals were used as received without further purification, and all aqueous solutions were prepared with ultrapure water. Cyanuric Acid ($C_3H_3N_3O_3$, 98.0%), benzoguanamine ($C_9H_9N_5$, 98.0%) and diclofenac sodium ($C_{14}H_{10}C_{12}NNaO_2$, 98.0%) were purchased from Tokyo Chemical Industry Co. Sodium hydroxide (NaOH, 96%), ammonia solution ($NH_3 \cdot H_2O$, 25.0%–28.0%), cobalt sulfate heptahydrate ($CoSO_4 \cdot 7H_2O$, 99.5%) and sodium acetate anhydrous (CH_3COONa, 99.0%) were obtained from Sinopharm Chemical Reagent Co. 5-tert-Butoxycarbonyl-5-methyl-1-pyrroline-N-oxide (BMPO, 99.0%) was purchased from DOJINDO. Oxone and 5,5-dimethyl-1-pyrroline-N-oxide (DMPO, >97.0%) were purchased from Sigma-Aldrich, Inc.

2.2. Synthesis of the photocatalysts

The g-C_3N_4 powder was synthesized by thermal polycondensation method. In a synthesis run, 3.8724 g cyanuric acid and 5.6163 g benzoguanamine were added into 95 mL ultrapure water and stirred for 6 h. Then, the suspensions were centrifuged (7000 rpm, 15 min) to collect the precursor and froze-dried for 3 days. The resulting powder was heated at a rate of 3 °C/min from ambient temperature to 500 °C in a tube furnace filled with inert nitrogen gas. The further process was carried out at 500 °C for 2 h. The final product was grounded into powder for further use.

The Co_3O_4 nanoparticles were synthesized by a hydrothermal method [23,24]. In a typical process, 1.4000 g of cobalt sulfate heptahydrate was dissolved in 25.0 mL water followed by extra of 30.0 mL of 0.33 M sodium hydroxide as well as 4.0 mL ammo-

nia solution. Then, the mixed solution was placed into a stainless steel autoclave and treated at 120 °C for 12 h. The precursors were collected by centrifugation, washing and drying. Then the final products were obtained by heating precursors in air at 450 °C for 3 h.

The preparation of the Co_3O_4-g-C_3N_4 hybrids was as follows: 3.8724 g cyanuric acid, 5.6163 g benzoguanamine and different amounts of Co_3O_4 were mixed together to form precursors and marked as 0.00 wt%, 0.02%, 0.20%, 2.00%, and 4.00%, respectively. Then, it was froze and dried. To further investigate the photoelectrochemical properties of Co_3O_4-g-C_3N_4 photocatalyst, indium-tin oxide (ITO) was used as electrode substrate material for fabricating Co_3O_4-g-C_3N_4/ITO composites electrode. A piece of cleaned ITO substrate was placed into crucible, with conductive side facing up and precursors putting on it. Subsequently, it was heated at a rate of 3 °C/min from ambient temperature to 500 °C in a tube furnace filled with inert nitrogen gas. Finally, the Co_3O_4-g-C_3N_4 hybrids powders and Co_3O_4-g-C_3N_4/ITO photoelectrodes were obtained at the same time.

2.3. Characterization

Thermo-gravimetric (TGA) measurements were performed on a Mettler TGA-1 thermogravimetric analyzer in O_2 atmosphere with a heating rate of 10 °C/min up to 1000 °C. The X-ray diffraction (XRD) was performed on an X'Pert PRO MPD system with Cu Kα radiation ($\lambda = 0.15418$ nm). Transmission electron microscopy (TEM) (Hitachi H7500, Japan) and field emission scanning electron microscopy (FESEM) (Hitachi SU-8020, Japan) with energy dispersive X-ray spectrum (EDX) were carried out to obtain the morphology and microstructure images. High resolution TEM (HRTEM) was performed on a JEOL JEM-2100F microscope at 200 kV. Diffuse reflection spectra (DRS) were performed on a spectrophotometer with an integrating sphere (Hitachi 3010, Japan) by using $BaSO_4$ as the reflectance standard to evaluate the optical absorbance of samples. X-ray photoelectron spectroscopy (XPS) was obtained using a Phi Quantern instrument. The binding energies were calibrated with C 1s = 284.8 eV. Photoluminescence spectra (PL) of the samples were performed on a fluorescence spectrometer (JASCO FP-6500).

The photoelectrical properties were measured using 0.05 M Na_2SO_4 as an electrolyte solution on a CHI 660 B electrochemical workstation with a three-electrode cell system including a reference electrode (saturated calomel electrode, SCE), a working electrode (Co_3O_4-g-C_3N_4/ITO) and a counter electrode (Pt wire). The visible light was acquired from a 300 W electric power and 50 W luminous power Xe lamp (BoPhilae technology Co., LTD, Beijing) with 420 nm cutoff filter. Chopped-light amperometric I-t characterizations were evaluated at an applied potential of 1.0 V under chopped light irradiation (light on or off cycles: 50 s). Electrochemical impedance spectroscopy (EIS) was conducted with 0.05 M Na_2SO_4 under the open-circuit potential (OCP) and visible light. The AC voltage amplitude was 5 mV and frequency range was from 100 000–0.01 Hz.

2.4. Photocatalytic degradation experiment

Photocatalytic degradation of DCF in the presence of PMS was performed under visible light obtained from a 300 W electric power and 50 W luminous power Xe lamp with 420 nm cutoff filter. The initial pH value of DFC (10 mg/L) was about 6.7. The pH values of DFC (10 mg/L) were adjusted by 0.1 M H_2SO_4 and 0.1 M NaOH. In each run, 100 mL of DCF (10 mg/L) containing 50 mg of a catalyst was transferred into the reactor. Prior to irradiation and addition of appropriate PMS into the reactor, an adsorption-desorption equilibrium between catalysts and DCF was achieved by stirring the
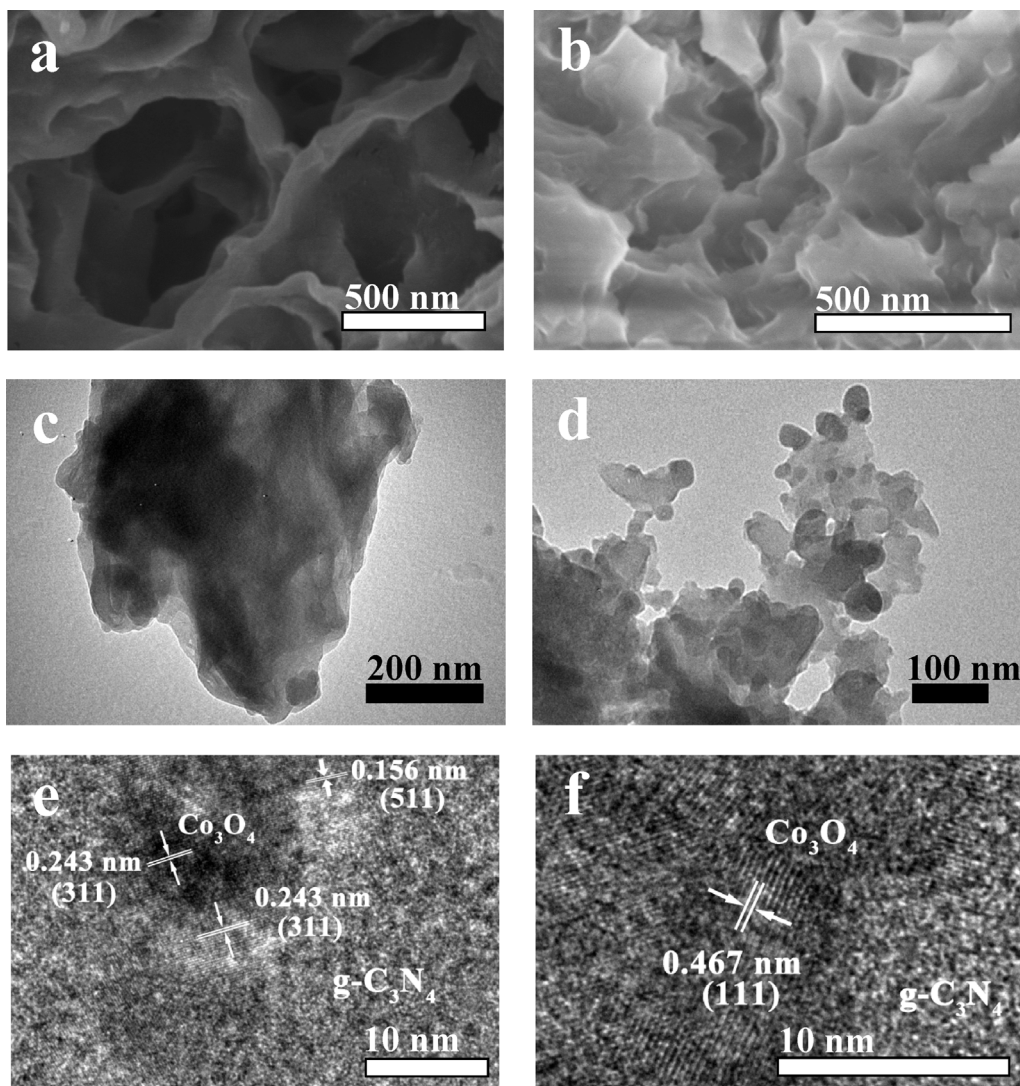
Fig. 2. SEM images of (a) g-C$_3$N$_4$ and (b) 0.20% Co$_3$O$_4$-g-C$_3$N$_4$, TEM images of (c) g-C$_3$N$_4$ and (d) 0.20% Co$_3$O$_4$-g-C$_3$N$_4$, and (e, f) HRTEM images of 0.20% Co$_3$O$_4$-g-C$_3$N$_4$.
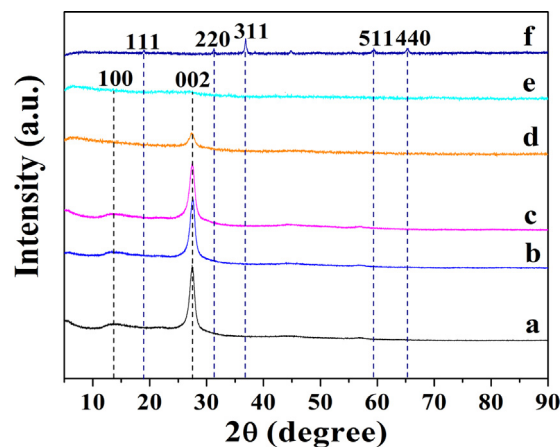
mixture in the dark for 0.5 h. The mixture was taken from the reactor and filtered (0.22 μm) to remove the particles with adding methanol to quench the radicals for HPLC (Shimadzu LC-20AT, Tokyo, Japan) analysis at set intervals. The temperature of AC-C18 column was set at 35 °C with a UV detector at 276 nm. The mobile phase was 60% of methanol and 40% of sodium acetate-acetic acid buffer solution which was adjusted to pH 5.00 at a flow rate of 1.0 mL/min.

A Bruker model ESR A300-10/12 spectrometer equipped with a quanta-Ray Nd: YAG laser system was carried out to obtain EPR signals of active radicals using DMPO and BMPO as spin-trapping agents. In order to detect the active species, radical scavengers were added into the reactor, including 0.05 M (0.46 mL) *tert*-butyl alcohol (TBA) for scavenging the $^\bullet$OH and 0.05 M (0.29 mL) ethanol (EtOH) for scavenging both SO$_4$$^{\bullet-}$ and $^\bullet$OH radicals.

3. Results and discussion

3.1. Characterization of the Co$_3$O$_4$ modified g-C$_3$N$_4$ catalyst

To accurately estimate the Co$_3$O$_4$ contents in Co$_3$O$_4$-g-C$_3$N$_4$ hybrids, TGA measurements were analyzed as shown in Fig. S1. Two mass loss steps are shown in the TGA curves for Co$_3$O$_4$-g-C$_3$N$_4$ samples. The first mass loss step at 500–700 °C is ascribed

Fig. 1. XRD patterns of pure g-C$_3$N$_4$ (a) and Co$_3$O$_4$ (f), and the Co$_3$O$_4$-g-C$_3$N$_4$ composite photocatalysts: 0.02%, 0.20%, 2.00%, 4.00% (b–e).

to the decomposition of g-C$_3$N$_4$ [25]. The second mass loss appears at 910–950 °C, which is attributed to decomposition of Co$_3$O$_4$ [26]. Therefore, the residuals between 700 and 910 °C are Co$_3$O$_4$, which weight percentages are calculated to be 0.00 wt%,
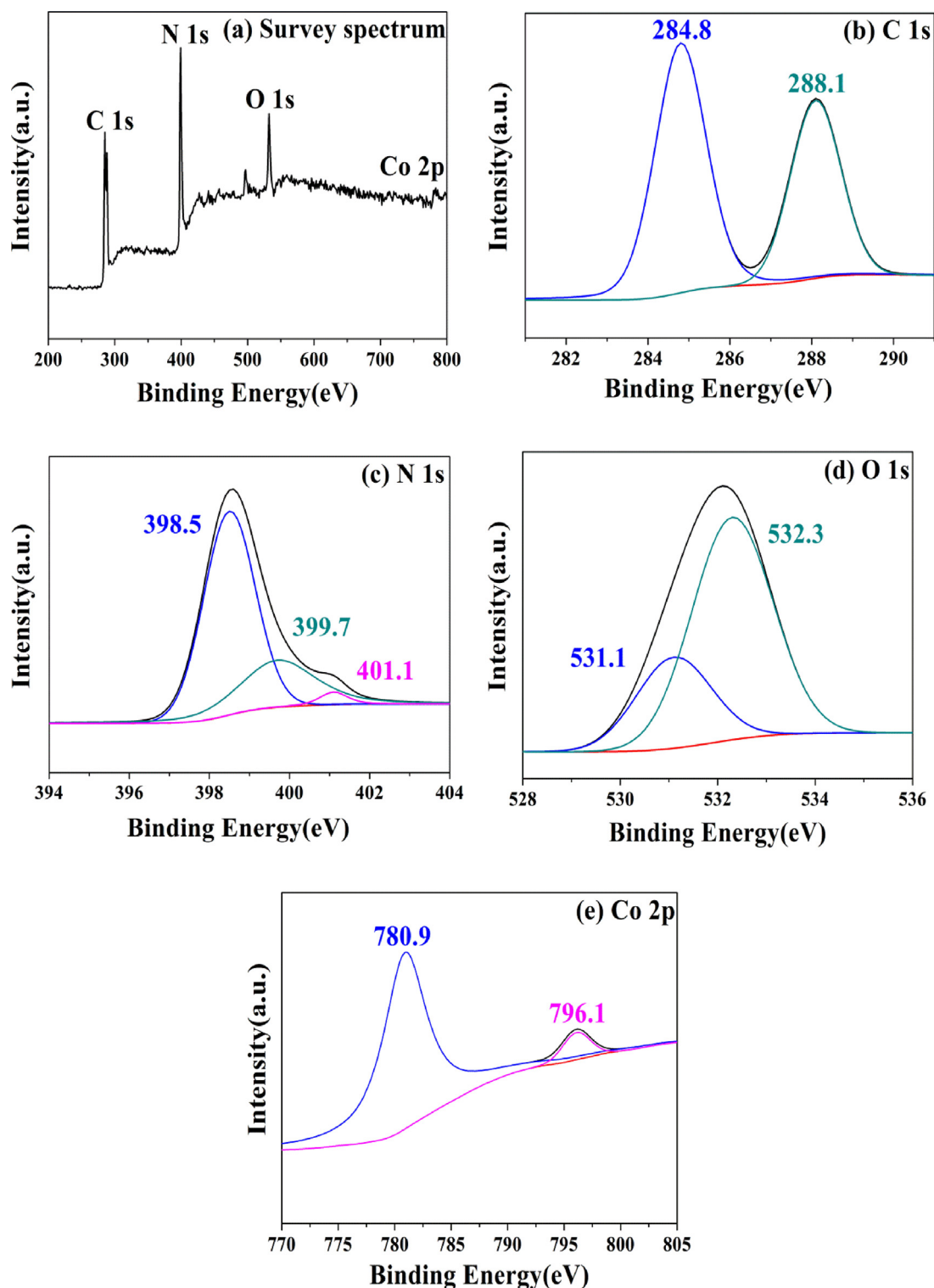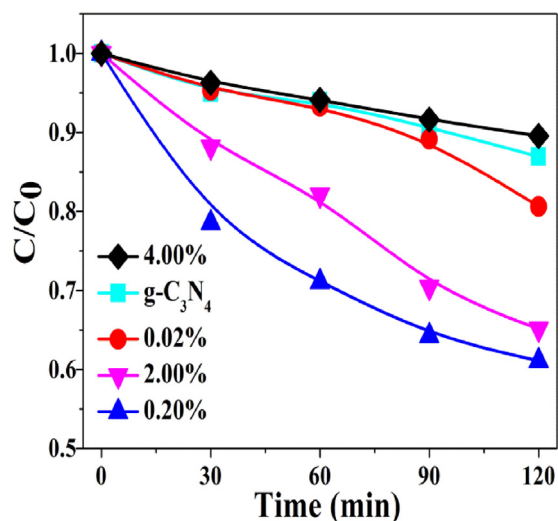
Fig. 3. XPS spectra of the 0.20% Co_3O_4-g-C_3N_4: (a) survey spectrum; (b) C 1s; (c) N 1s; (d) O 1s; (e) Co 2p.

0.77 wt%, 1.06 wt%, 7.79 wt%, and 13.75 wt%, for the nominal doping weight percentages with 0.00 wt%, 0.02 wt%, 0.20 wt%, 2.00 wt%, and 4.00 wt%, respectively.

XRD patterns of the Co_3O_4-g-C_3N_4 composites with different amounts of Co_3O_4 are shown in Fig. 1, together with the individual g-C_3N_4 and Co_3O_4. The vertical dotted lines in black correspond to the (100) and (002) planes of g-C_3N_4. The vertical dotted lines in blue correspond to the diffraction peaks of Co_3O_4. For the individual

g-C_3N_4 sample, the strongest peak at 27.5° is a typical interlayer stacking peak of aromatic systems, indexed for graphitic structure as the (002) peak [16,27]. The diffraction peaks of the individual Co_3O_4 are in good agreement with the (111), (220), (311), (511), and (440) planes which are reported in the literature [23,24]. With the increase of the Co_3O_4 amount, the diffraction peak (002) of g-C_3N_4 is also present in the pattern of Co_3O_4-g-C_3N_4 composite and gradually appears weaker, which indicates that g-C_3N_4 has been

Fig. 4. Degradation of DCF under visible light irradiation in the presence of Co_3O_4-g-C_3N_4 samples with different Co_3O_4 doping amount. Reaction conditions: $[DCF]_0 = 10\,mg/L$, $[catalyst]_0 = 0.5\,g/L$.

restrained by Co_3O_4 in the formation of the crystals. The diffraction peaks of Co_3O_4 in the hybrids are not observed which maybe due to its good dispersion, small particle size and low contents [11,12,22].

The morphology and microstructure of the Co_3O_4-g-C_3N_4 hybrids were investigated by SEM, TEM and HRTEM. As exhibited in Fig. 2a, porous structures of the g-C_3N_4 are observed, which can be caused by the released gas (CO_2, H_2O, NH_3) during the thermal polymerization process [21] and may enhance the photocatalytic activity. The porous structures can still be retained upon the coupling of Co_3O_4 (Fig. 2b). The TEM images of g-C_3N_4 and Co_3O_4-g-C_3N_4 are shown in Fig. 2c and d. Individual g-C_3N_4 sample displays a typical layer structure as reported [28]. For Co_3O_4-g-C_3N_4 hybrids, dark Co_3O_4 species with a 10–50 nm diameter are distributed on the layer g-C_3N_4. Fig. 2e and f clearly show the existence of Co_3O_4 in the Co_3O_4-g-C_3N_4 samples. The HRTEM images show the lattice spacings existing in Co_3O_4-g-C_3N_4 samples are 0.156, 0.243, and 0.467 nm, which can be assigned to (511), (311), and (111) planes of Co_3O_4, respectively. After ultrasonication process, the interaction still exists between the Co_3O_4 nanoparticles and the g-C_3N_4 layer, confirming its stability [29]. EDX mapping analysis was carried out to illustrate the element distribution in the Co_3O_4-g-C_3N_4 sample. As shown in Fig. S2, the N element is evenly distributed in the whole sample, and the distri-

bution of Co is in good agreement with the brightness in the STEM image.

The XPS spectra are shown in Fig. 3 to analyze chemical composition of the Co_3O_4-g-C_3N_4 composites. Obvious photoelectron peaks of C, N, O, and Co elements are observed in Fig. 3a from the surface of 0.20% Co_3O_4-g-C_3N_4. The high-resolution C 1s XPS spectrum reveals two evident signals (Fig. 3b). The peaks at 284.8 and 288.1 eV correspond to the structure of graphite-like sp^2 C—C and N-sp^3C (N—C=N) [14,19,21,28,30], respectively. The curves of N 1s comprises three peaks with 398.5 eV peak corresponding to sp^2-hybridized nitrogen (C—N=C) existed in the g-C_3N_4 and the other two weak peaks corresponding to sp^3 C—N and C—N—H bonds (Fig. 3c) [14,21], respectively. The high resolution XPS spectrum of O 1 s (Fig. 3d) shows two different peaks at 531.1 and 532.3 eV, corresponding to lattice oxygen atoms in the Co_3O_4 [31] and external water molecule [14], respectively. As displayed in Fig. 3e, the two peaks at 796.1 and 780.9 eV are the signals of Co $2p_{1/2}$ and Co $2p_{3/2}$ spin orbits [22]. The XPS results show the chemical state of g-C_3N_4 and Co_3O_4 in the hybrids, which quite fits in with the HRTEM results.
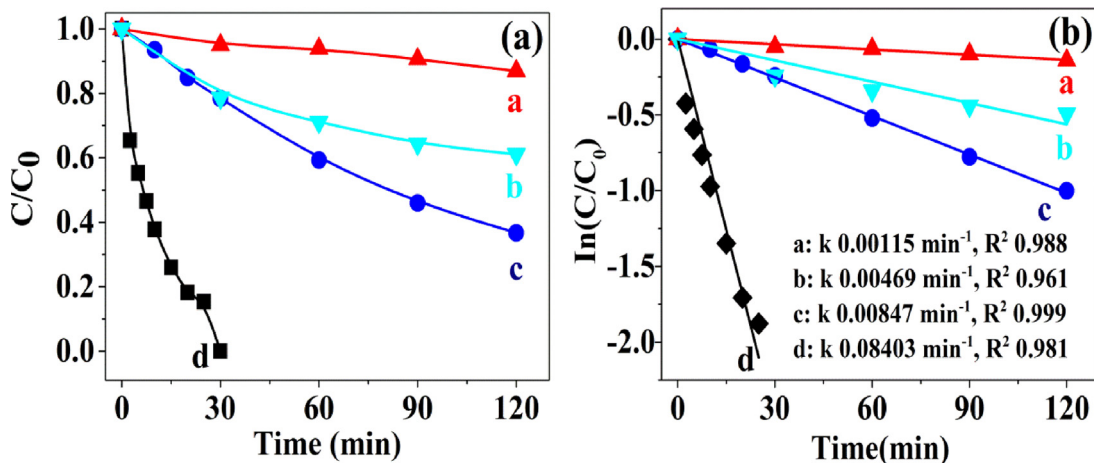
3.2. Diclofenac sodium degradation

3.2.1. Photocatalytic activity

The photocatalytic activities of the Co_3O_4-g-C_3N_4 composites with different Co_3O_4 weight percentages were firstly estimated by the removal of DCF under visible light irradiation (Fig. 4). Only 13% DCF is degraded after 120 min with pure g-C_3N_4 under visible light. The photocatalytic performance is enhanced after modification by Co_3O_4. 0.20% Co_3O_4-g-C_3N_4 exhibits the highest photocatalytic activity among all samples and 40% of DCF is degraded after 120 min. Overall, due to the synergistic effect between the Co_3O_4 and g-C_3N_4, the hybrids have a great improvement in photocatalysis activity [19,21,22,28,29]. However, 4.00% Co_3O_4-g-C_3N_4 exhibits lower photocatalytic activity compared with pristine g-C_3N_4, which may be explained by the agglomeration and lower dispersibility of Co_3O_4 species, resulting in the low migration and separation rate of the photogenerated charges [21,22,28,29]. Therefore, an appropriate doping level and dispersion of Co_3O_4 in the Co_3O_4-g-C_3N_4 composites are critical. The as-prepared 0.20% Co_3O_4-g-C_3N_4 composite was selected for further studies for PMS activation.

3.2.2. Synergetic degradation of DCF in the presence of PMS

As shown in Fig. 5a, the PMS activation performance of the prepared photocatalyst for DCF degradation is exhibited. For the

Fig. 5. Images of DCF degradation (a) and chemical kinetics-rate equations (b) with different systems of (a) g-C_3N_4/Vis; (b) 0.20% Co_3O_4-g-C_3N_4/Vis; (c) g-C_3N_4/PMS/Vis; (d) 0.20% Co_3O_4-g-C_3N_4/PMS/Vis. Reaction conditions: $[DCF]_0 = 10\,mg/L$, $[catalyst]_0 = 0.5\,g/L$, $[PMS]_0 = 0.1\,mM$, Vis, at room temperature.

g-C_3N_4/PMS/Vis system, 60% DCF can be removed after 120 min, which is much higher than the g-C_3N_4/Vis system. The results indicate that g-C_3N_4 can activate PMS under visible light irradiation. By contrast, DCF can be completely removed in 30 min by 0.20% Co_3O_4-g-C_3N_4 under the same condition. These results suggest that the Co_3O_4-g-C_3N_4 composites can generate a synergistic effect in the PMS activation process compared to the pure g-C_3N_4, which is similar to those of $MnFe_2O_4$-rGO, $CoFe_2O_4$-rGO, Co_3O_4-Graphene, MnO_2-$ZnFe_2O_4$ and $CuFeO_2$ catalysts reported in the literatures [4–6,9,10].

As shown in Fig. 5b, the DCF degradation follows a pseudo-first-order kinetic. The rate constant is estimated to be 0.08403 min^{-1} ($R^2 = 0.981$) in the 0.20% Co_3O_4-g-C_3N_4/PMS/Vis system. By contrast, corresponding to g-C_3N_4/Vis, 0.20% Co_3O_4-g-C_3N_4/Vis, and g-C_3N_4/PMS/Vis system, the rate constants are 0.00115 ($R^2 = 0.988$), 0.00469 ($R^2 = 0.961$), and 0.00847 min^{-1} ($R^2 = 0.999$), respectively. These results strongly confirm the enhancement of DCF degradation in 0.20% Co_3O_4-g-C_3N_4/PMS/Vis system compared to that in the g-C_3N_4/PMS/Vis system or 0.20% Co_3O_4-g-C_3N_4/Vis system.

3.2.3. Effect of operation parameters

The concentration of DCF and PMS as well as the initial pH of the solution were selected as control variables to explore the suitable value of 0.20% Co_3O_4-g-C_3N_4/PMS/Vis system for DCF removal.
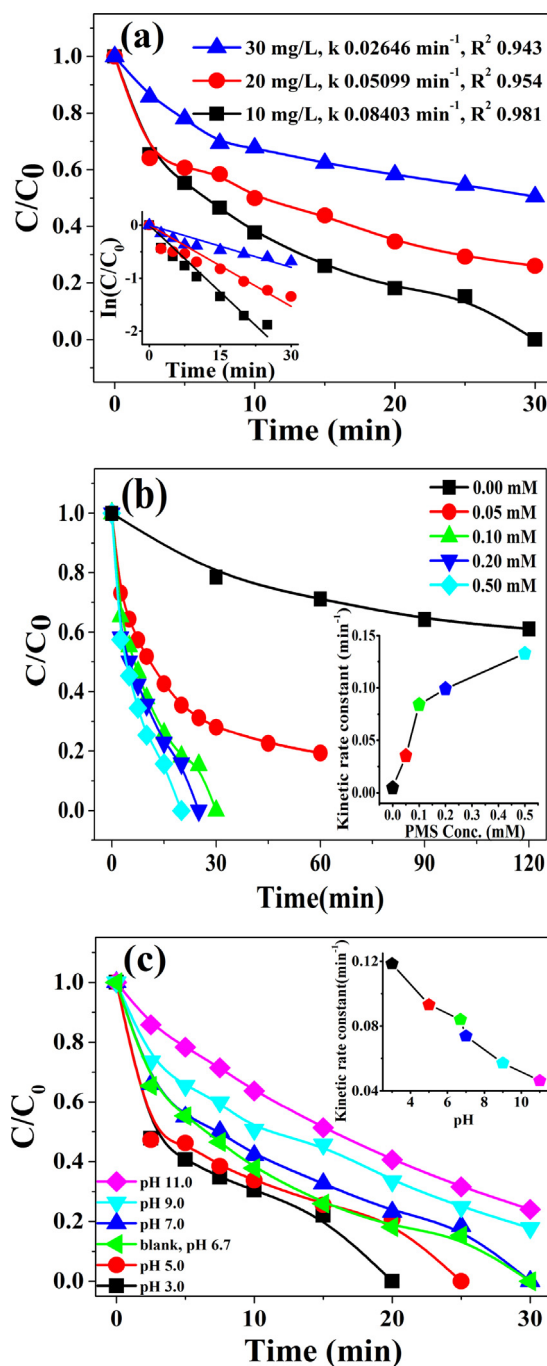
As shown in Fig. 6a, with the increased DCF concentration from 10 to 30 mg/L, the removal rate decreases and the first order-kinetic constant is decreased from 0.08403 ($R^2 = 0.981$) to 0.02646 min^{-1} ($R^2 = 0.943$), which may be explained that a certain amount of PMS and catalyst can generate the same active species to remove DCF. Lower amount of initial pollutants can achieve higher removal rate at the same time.

The effect of PMS concentration is exhibited in Fig. 6b. Without PMS, 40% of DCF is removed within 120 min. When 0.10 mM PMS is added, almost 100% DCF is removed within 30 min, resulting from the more generated reactive species with the higher PMS concentration. When PMS concentration is increased to 0.50 mM, only a slight improvement of DCF removal is observed. Therefore, 0.10 mM PMS concentration was selected in the subsequent experiments.

As exhibited in Fig. 6c, the removal of DCF is affected by the initial pH of the solution. With the pH increases from 3 to 11, the first order-kinetic constant is decreased from 0.11845 ($R^2 = 0.925$) to 0.04632 min^{-1} ($R^2 = 0.999$). At pH 3, almost 100% DCF is removed within 20 min. At pH 7, the degradation rate becomes slower with 30 min to achieve a complete removal. By contrast, at pH 11, only 75% removal can be achieved within 30 min, which may be ascribed to that the $SO_4^{\bullet-}$ would react with OH^- to form $^{\bullet}OH$ with a relatively weaker redox potential in alkaline conditions [32]. Meanwhile, at the initial solution pH of 6.7 without the pH regulation, nearly complete DCF removal is achieved at 30 min. And the pH variations with the reaction evolution under different conditions are investigated. It can be observed that the solution pH decreases as the reaction proceeds under both the acid and alkaline conditions. For instance, when the pH values of the original solution system are 9.0, 7.0, and 5.0, the pH of the solution after 30 min are 5.1, 4.1, and 3.9, respectively. This phenomenon is caused by the acidification stemming from the transformation of $SO_4^{\bullet-}$ to $^{\bullet}OH$, which consumes OH^- in the solution.

3.3. Photoelectrochemical properties of the prepared Co_3O_4-g-C_3N_4 composites

To evaluate the contribution of Co_3O_4 to the separation and migration efficiency of photogenerated carriers in Co_3O_4-g-C_3N_4 composites, the photocurrent responses under alternatively visi-

Fig. 6. Influence of (a) DCF concentration: [PMS]$_0$ = 0.1 mM, pH = 6.7, (b) PMS concentration: [DCF]$_0$ = 10 mg/L, pH = 6.7 and (c) initial solution pH: [DCF]$_0$ = 10 mg/L, [PMS]$_0$ = 0.1 mM on the DCF degradation with 0.20% Co_3O_4-g-C_3N_4/PMS/Vis system (the insert is chemical kinetics-rate image, respectively). Reaction conditions: [catalyst]$_0$ = 0.5 g/L, Vis irradiation.

ble light illumination on and off cycles, EIS spectra, PL spectra and UV–vis DRS spectra were investigated.

As shown in Fig. 7a, a sensitive photoelectric response is observed for each on-off run in both pure g-C_3N_4 and 0.20% Co_3O_4-g-C_3N_4. The photocurrents for the 0.20% Co_3O_4-g-C_3N_4 composite sample exhibits an obvious enhancement compared to pure g-C_3N_4 or Co_3O_4, which indicates that the former has lower recombination efficiency of photogenerated electron-hole pairs [17,33]. The amperometric curve of Co_3O_4 electrode slowly reaches a steady state compared to those of g-C_3N_4 or 0.20% Co_3O_4-g-C_3N_4 photoelectrodes, which indicates that Co_3O_4 has
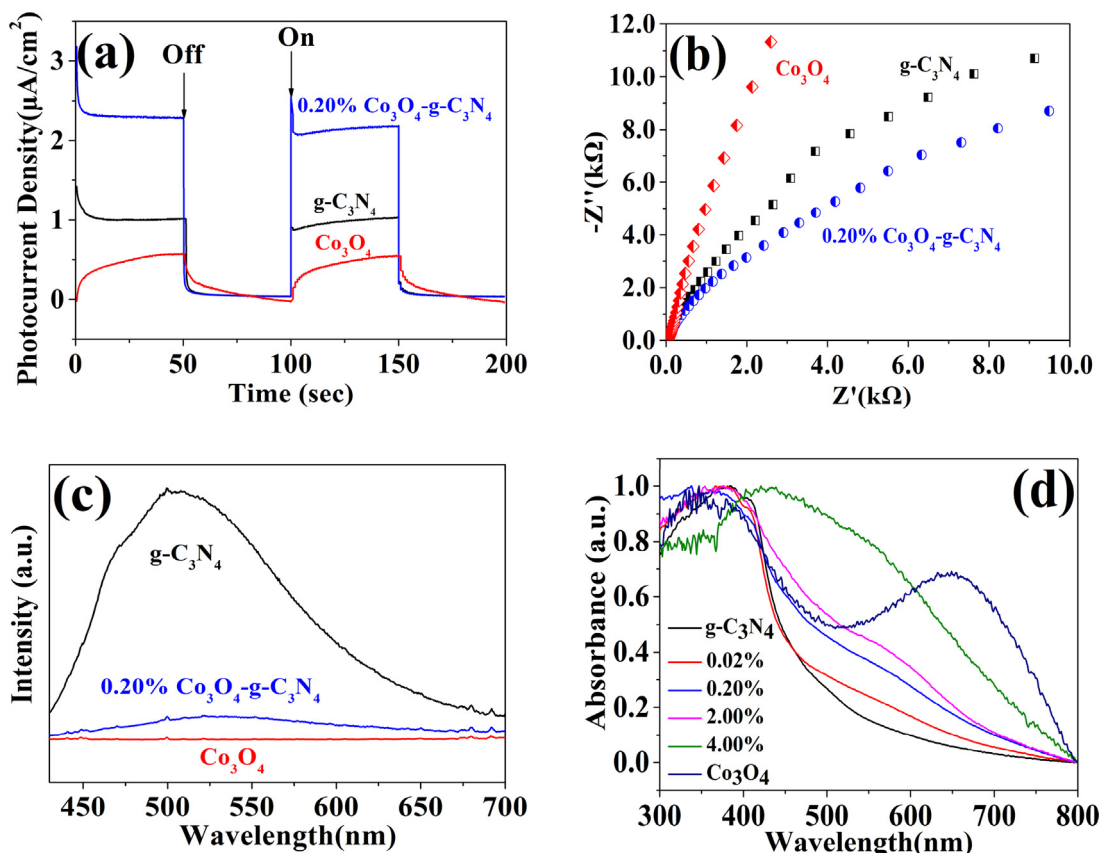
Fig. 7. Periodic on/off photocurrent responses (a), EIS spectra of photoanodes (b), PL spectra (c) and UV–vis DRS spectra (d).

weak light responsiveness [34]. As shown in Fig. 7b, 0.20% Co_3O_4-g-C_3N_4 composite sample has a lower charge transfer resistance with the smaller Nyquist semicircle compared to g-C_3N_4 or Co_3O_4, which indicates the former has the superiority in the conductivity and separation efficiency of the photo-charges [17,19,35]. The PL spectrum revealing the migration, transfer, and recombination processes of photoinduced electron-hole pairs with excitation wavelength at 400 nm is presented in Fig. 7c. The 0.20% Co_3O_4-g-C_3N_4 sample shows the weaker intensity than g-C_3N_4, which indicates that the former has an improvement ability in the separation of photo-electrons and holes [19,22,28]. However, Co_3O_4 has the weakest intensity at 430–700 nm, which can be explained by that Co_3O_4 has a broad emission above 700 nm and the intensity of peak is much lower than g-C_3N_4 as reported [36]. These results all show that Co_3O_4-g-C_3N_4 composites have an obvious superiority in the migration and separation of photogenerated charges.

UV–vis DRS was measured to identify the optical absorption of the samples (Fig. 7d). The photocatalytic activity can be reflected by the absorption edge of samples. The absorption edge is about 477 nm for g-C_3N_4, which is significant to the utilization of visible light. With the increase of the Co_3O_4 loading, red shift of the hybrids is observed, resulting in the enhanced optical absorption of the samples.
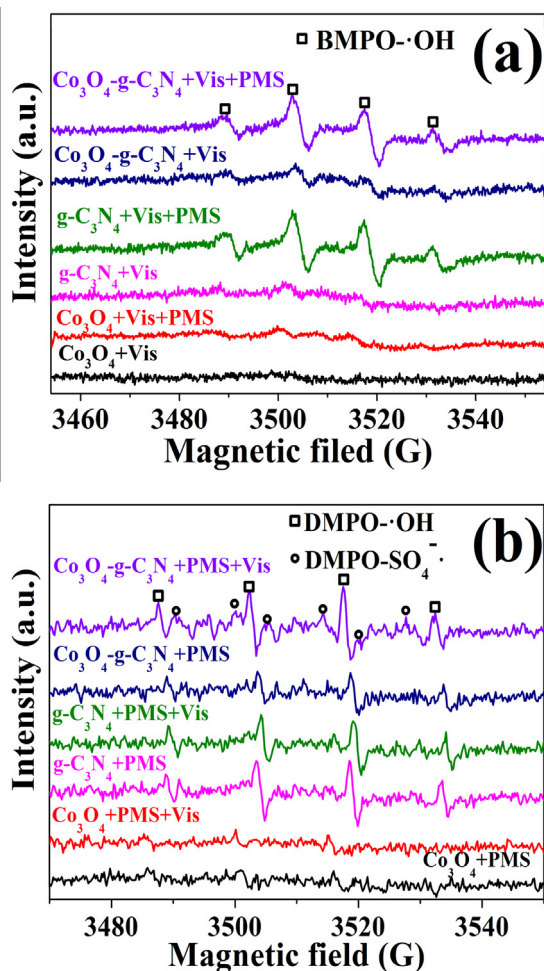
3.4. Involved active species

As shown in Fig. 8a, EPR spectra in different systems were measured to explore the effect of catalyst and PMS on the generation of active radicals. With the addition of 0.1 mM PMS to the photocatalytic system, the $^\bullet$OH signals [37] are observed in

0.20% Co_3O_4-g-C_3N_4/PMS/Vis and g-C_3N_4/PMS/Vis, resulting in the enhancement of photocatalytic degradation of DCF. The results show that PMS can be activated by g-C_3N_4 and 0.20% Co_3O_4-g-C_3N_4 to generate $^\bullet$OH, which may be from the reaction between $SO_4^{\bullet-}$ and H_2O/OH^-. However, no ESR signals of $SO_4^{\bullet-}$ are observed in 0.20% Co_3O_4-g-C_3N_4/PMS/Vis or g-C_3N_4/PMS/Vis system in the presence of 0.1 mM PMS with the 0.08 M DMPO as spin trapping agent. Therefore, to identify the active radicals, 20 mM PMS is added together with DMPO as spin trapping agent.

Both $^\bullet$OH [38] and $SO_4^{\bullet-}$ [39] are detected in different systems as shown in Fig. 8b. On the one hand, the g-C_3N_4/PMS and 0.20% Co_3O_4-g-C_3N_4/PMS systems can activate PMS to generate $SO_4^{\bullet-}$ and $^\bullet$OH without visible light irradiation. On the other hand, PMS can also be activated by g-C_3N_4 and 0.20% Co_3O_4-g-C_3N_4 under visible light, and the intensity of $SO_4^{\bullet-}$ and $^\bullet$OH signals increases compared to the g-C_3N_4/PMS and 0.20% Co_3O_4-g-C_3N_4/PMS systems. The visible light, which can induce catalyst to generate photo-electron, is significant to the PMS activation.

For comparison, Co_3O_4/PMS and Co_3O_4/PMS/Vis systems were also analyzed by EPR. To better study the role of Co_3O_4 in 0.20% Co_3O_4-g-C_3N_4 composites, 0.007 g/L dosage of Co_3O_4 was selected based on the about equivalent Co_3O_4 content of 0.5 g/L 0.20% Co_3O_4-g-C_3N_4 composites as similar reported [40]. With other conditions unchanged, the EPR spectra are shown in Fig. 8. There are no evident $^\bullet$OH signals in Co_3O_4/Vis or Co_3O_4/PMS/Vis system with 0.1 mM PMS addition (Fig. 8a). The similar results are obtained and no obvious $^\bullet$OH or $SO_4^{\bullet-}$ signals are observed in Co_3O_4/PMS or Co_3O_4/PMS/Vis systems with 20 mM PMS addition (Fig. 8b). These results can be attributed to that pure Co_3O_4 nanoparticles are more likely to aggregate compared to the Co_3O_4 nanoparticles in 0.20% Co_3O_4-g-C_3N_4 composites [11]. Therefore, the activation of PMS

Fig. 8. EPR spectra under various conditions. Reaction condition: (a) [g-C$_3$N$_4$]$_0$ = 0.50 g/L, [0.20% Co$_3$O$_4$-g-C$_3$N$_4$]$_0$ = 0.50 g/L, [Co$_3$O$_4$]$_0$ = 0.007 g/L, [PMS]$_0$ = 0.1 mM, [BMPO] = 0.08 M. (b) [g-C$_3$N$_4$]$_0$ = 0.50 g/L, [0.20% Co$_3$O$_4$-g-C$_3$N$_4$]$_0$ = 0.50 g/L, [Co$_3$O$_4$]$_0$ = 0.007 g/L, [PMS]$_0$ = 20 mM, [DMPO] = 0.08 M.

is not evident due to less active sites of Co$_3$O$_4$ nanoparticles in Co$_3$O$_4$/Vis and Co$_3$O$_4$/PMS/Vis systems.

Quenching tests were performed by using EtOH and TBA to differentiate SO$_4$$^{\bullet-}$ from $^{\bullet}$OH [5,8]. As shown in Fig. 9, both EtOH and TBA inhibit the removal of DCF. However, the removal efficiency
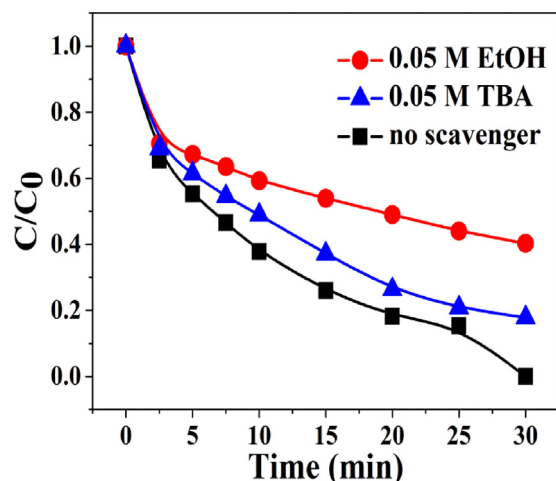
Fig. 9. Effect of radical scavngers on the degradation of DCF. Reaction conditions: [DCF]$_0$ = 10 mg/L, [0.20% Co$_3$O$_4$-g-C$_3$N$_4$]$_0$ = 0.5 g/L, [PMS]$_0$ = 0.1 mM, Vis irradiation.

Table 1
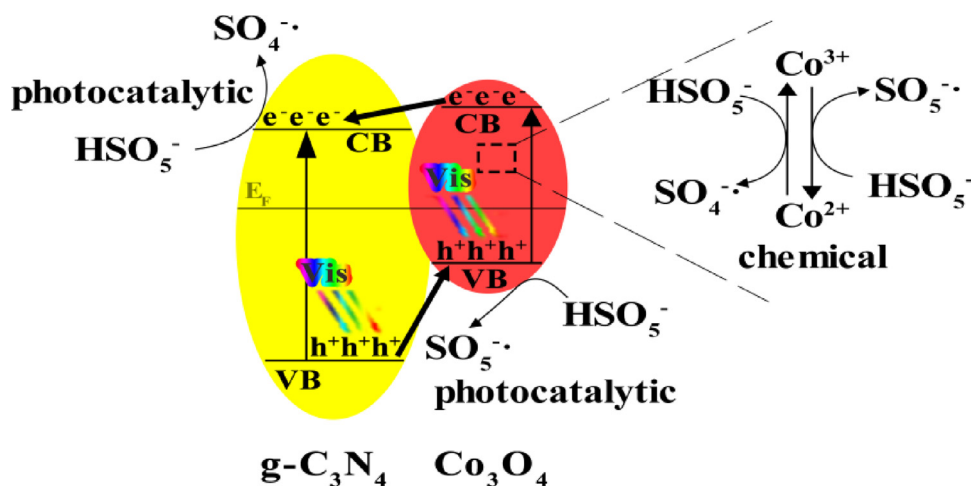The mechanism of PMS activation by Co$_3$O$_4$-g-C$_3$N$_4$ for pollutants degradation under visible light irradiation.

Photocatalytic activation	Chemical activation [8]
Co$_3$O$_4$-g-C$_3$N$_4$ + hv → e$^-$ + h$^+$	Co^{2+} + HSO$_5$$^-$ → Co^{3+} + SO$_4$$^{-\bullet}$ + OH$^-$
HSO$_5$$^-$ + e$^-$ → SO$_4$$^{-\bullet}$ + OH$^-$	Co^{3+} + HSO$_5$$^-$ → Co^{2+} + SO$_5$$^{-\bullet}$ + H$^+$
HSO$_5$$^-$ + h$^+$ → SO$_5$$^{-\bullet}$ + H$^+$	SO$_4$$^{-\bullet}$ + pollutants → products
SO$_4$$^{-\bullet}$ + pollutants → products	

of DCF is 60% with 0.05 M EtOH, whereas 80% removal is achieved with 0.05 M TBA, which indicates that both SO$_4$$^{\bullet-}$ and $^{\bullet}$OH radicals contribute to the removal of DCF.

3.5. A proposed enhanced mechanism

On the basis of the above results, a mechanism is proposed and described in Table 1 and Fig. 10. Co$_3$O$_4$ is a characteristic p-type semiconductor [24,41], while g-C$_3$N$_4$ is n-type [20]. For pure Co$_3$O$_4$ and g-C$_3$N$_4$, both conduction band (CB) bottom and valence band (VB) top of g-C$_3$N$_4$ are more negative than that of Co$_3$O$_4$ [24,28]. However, in the Co$_3$O$_4$-g-C$_3$N$_4$ composites, inner electric field should be also taken into consideration when analyzing the migration process of photo-electrons and holes [20,24,28,41,42]. Under visible light, both Co$_3$O$_4$ and g-C$_3$N$_4$ can be stimulated to generate photo-induced electrons and holes. The electrons are

Fig. 10. Schematic diagrams for the possible photocatalytic- and chemical-activation mechanism of the Co$_3$O$_4$-g-C$_3$N$_4$ composite with PMS under visible light irradiation.

transferred from the conduction band of Co_3O_4 to g-C_3N_4, while the holes are transferred from the valence band of g-C_3N_4 to Co_3O_4. And the migration of photo-induced electrons and holes are both enhanced as illustrated in Fig. 10. Therefore, the *p-n* heterojunction of the Co_3O_4-g-C_3N_4 samples inhibits the recombination of the photogenerated charges. Meanwhile, the Co_3O_4 as a transitional metal oxide in the hybrid composites can activate PMS to generate $SO_4^{\bullet-}$. Therefore, it is proposed that the Co_3O_4-g-C_3N_4 heterojunction can generate a synergistic effect of the photocatalytic- and chemical-processes in the PMS activation, leading to the increased generation amount of $SO_4^{\bullet-}$. As a result, DCF is efficiently degraded.

4. Conclusions

In this paper, Co_3O_4-g-C_3N_4 heterojunction photocatalysts with different Co_3O_4 doping amount were fabricated. The 0.20% Co_3O_4-g-C_3N_4 showed the highest photocatalytic activity toward the degradation of DCF and 40% DCF with the initial concentration of 10 mg/L could be removed in 120 min. By contrast, nearly 100% of DCF was removed within 30 min by 0.20% Co_3O_4-g-C_3N_4 catalyst in the presence of PMS, suggesting a synergistic effect between the photocatalytic and chemical activation of PMS. Based on the EPR spectra and quenching tests, it was found that both $^{\bullet}OH$ and $SO_4^{\bullet-}$ contributed to the removal of DCF in 0.20% Co_3O_4-g-C_3N_4/PMS/Vis system. The photogenerated electrons and Co_3O_4 as a transitional metal oxide in the hybrid composites could jointly activate PMS to generate $SO_4^{\bullet-}$, which leaded to the efficient DCF oxidation.

Acknowledgment

Appendix A. Supplementary data

Supplementary data associated with this article can be found, in the online version, at http://dx.doi.org/10.1016/j.apcatb.2017.07.016.

References

[1] S.H. Do, J.H. Jo, Y.H. Jo, H.K. Lee, S.H. Kong, Chemosphere 77 (2009) 1127–1131.
[2] Y. Ji, D. Kong, J. Lu, H. Jin, F. Kang, X. Yin, Q. Zhou, J. Hazard. Mater. 313 (2016) 229–237.
[3] S. Verma, S. Nakamura, M. Sillanpää, J. Chem. Eng. 284 (2016) 122–129.
[4] M. Wei, L. Gao, J. Li, J. Fang, W. Cai, X. Li, A. Xu, J. Hazard. Mater. 316 (2016) 60–68.
[5] Y. Feng, D. Wu, Y. Deng, T. Zhang, K. Shih, Environ. Sci. Technol. 50 (2016) 3119–3127.
[6] Y. Wang, H. Sun, H.M. Ang, M.O. Tade, S. Wang, ACS Appl. Mater. Interfaces 6 (2014) 19914–19923.
[7] E. Saputra, S. Muhammad, H. Sun, H.-M. Ang, M.O. Tadé, S. Wang, Appl. Catal. B-Environ. 154–155 (2014) 246–251.
[8] Y. Wang, L. Zhou, X. Duan, H. Sun, E.L. Tin, W. Jin, S. Wang, Catal. Today 258 (2015) 576–584.
[9] C. Wang, P. Shi, X. Cai, Q. Xu, X. Zhou, X. Zhou, D. Yang, J. Fan, Y. Min, H. Ge, W. Yao, J. Phys. Chem. C 120 (2016) 336–344.
[10] Y. Yao, Z. Yang, H. Sun, S. Wang, Ind. Eng. Chem. Res. 51 (2012) 14958–14965.
[11] H. Yang, K. Lv, J. Zhu, Q. Li, D. Tang, W. Ho, M. Li, S.A.C. Carabineiro, Appl. Surf. Sci. 401 (2017) 333–340.
[12] G. Zhou, H. Sun, S. Wang, H. Ming Ang, M.O. Ming Tadé, Sep. Purif. Technol. 80 (2011) 626–634.
[13] X. Wang, K. Maeda, A. Thomas, K. Takanabe, G. Xin, J.M. Carlsson, K. Domen, M. Antonietti, Nat. Mater. 8 (2009) 76–80.
[14] Y. Li, R. Wang, H. Li, X. Wei, J. Feng, K. Liu, Y. Dang, A. Zhou, J. Phys. Chem. C 119 (2015) 20283–20292.
[15] L. Zhou, H. Zhang, H. Sun, S. Liu, M.O. Tade, S. Wang, W. Jin, Catal. Sci. Technol. 6 (2016) 7002–7023.
[16] S.C. Yan, Z.S. Li, Z.G. Zou, Langmuir 25 (2009) 10397–10401.
[17] J. Xu, Y. Wang, Y. Zhu, Langmuir 29 (2013) 10566–10572.
[18] Y. Tao, Q. Ni, M. Wei, D. Xia, X. Li, A. Xu, RSC Adv. 5 (2015) 44128–44136.
[19] S. Kumar, T.B. Kumar, A. Baruah, V. Shanker, J. Phys. Chem. C 117 (2013) 26135–26143.
[20] D. Jiang, L. Chen, J. Zhu, M. Chen, W. Shi, J. Xie, Dalton Trans. 42 (2013) 15726–15734.
[21] Q. Li, N. Zhang, Y. Yang, G. Wang, D.H. Ng, Langmuir 30 (2014) 8965–8972.
[22] C. Han, L. Ge, C. Chen, Y. Li, X. Xiao, Y. Zhang, L. Guo, Appl. Catal. B-Environ. 147 (2014) 546–553.
[23] B. Wang, X.-Y. Lu, Y. Tang, J. Mater. Chem. A 3 (2015) 9689–9699.
[24] X. Chang, T. Wang, P. Zhang, J. Zhang, A. Li, J. Gong, J. Am. Chem. Soc. 137 (2015) 8356–8359.
[25] J.X. Sun, Y.P. Yuan, L.G. Qiu, X. Jiang, A.J. Xie, Y.H. Shen, J.F. Zhu, Dalton Trans. 41 (2012) 6756–6763.
[26] J. Gamonchuang, P. Poosimma, K. Saito, N. Khaorapapong, M. Ogawa, Colloid Surf. A 511 (2016) 39–46.
[27] F. Raziq, Y. Qu, M. Humayun, A. Zada, H. Yu, L. Jing, Appl. Catal. B-Environ. 201 (2017) 486–494.
[28] M. Xu, L. Han, S. Dong, ACS Appl. Mater. Interfaces 5 (2013) 12533–12540.
[29] L. Huang, H. Xu, Y. Li, H. Li, X. Cheng, J. Xia, Y. Xu, G. Cai, Dalton Trans. 42 (2013) 8606–8616.
[30] Y. Zhang, P. Zhang, Y. Huo, D. Zhang, G. Li, H. Li, Appl. Catal. B-Environ. 115–116 (2012) 236–244.
[31] NIST data base for XPS core levels.
[32] O.S. Furman, A.L. Teel, R.J. Watts, Environ. Sci. Technol. 44 (2010) 6423–6428.
[33] C. Feng, Z. Wang, Y. Ma, Y. Zhang, L. Wang, Y. Bi, Appl. Catal. B-Environ. 205 (2017) 19–23.
[34] X. Huang, T. Cao, M. Liu, G. Zhao, J. Phys. Chem. C 117 (2013) 26432–26440.
[35] X. Hao, Z. Jin, H. Yang, G. Lu, Y. Bi, Appl. Catal. B-Environ. 210 (2017) 45–56.
[36] W. Wang, J. Xu, ACS Appl. Mater. Interfaces 7 (2015) 415–421.
[37] W. He, Y.T. Zhou, W.G. Wamer, M.D. Boudreau, J.J. Yin, Biomaterials 33 (2012) 7547–7555.
[38] X. Li, J. Zhu, H. Li, Appl. Catal. B-Environ. 123–124 (2012) 174–181.
[39] M. Feng, R. Qu, X. Zhang, P. Sun, Y. Sui, L. Wang, Z. Wang, Water Res. 85 (2015) 1–10.
[40] Y. Lei, C.S. Chen, Y.J. Tu, Y.H. Huang, H. Zhang, Environ. Sci. Technol. 49 (2015) 6838–6845.
[41] M. Long, W. Cai, J. Cai, B. Zhou, X. Chai, Y. Wu, J. Phys. Chem. B 110 (2006) 20211–20216.
[42] R. Hao, G. Wang, H. Tang, L. Sun, C. Xu, D. Han, Appl. Catal. B-Environ. 187 (2016) 47–58.